AGU PUBLICATIONS

JGR

Journal of Geophysical Research: Solid Earth

RESEARCH ARTICLE
10.1002/2016JB013267

Special Section:
Slow Slip Phenomena and Plate Boundary Processes

Coupling on the northern Cascadia subduction zone from geodetic measurements and physics-based models

Lucile Bruhat[1] and Paul Segall[1]

[1] Department of Geophysics, Stanford University, Stanford, California, USA

Key Points:
- Physics-based approach to fit both the mean ETS displacements and decadal geodetic rates in northern Cascadia
- Models that acceptably fit geodetic data imply megathrust locked to near 20 km depth
- Below locked zone shear stresses decrease with time on decadal time scales

Supporting Information:
- Supporting Information S1
- Tables S1
- Tables S2

Correspondence to:
L. Bruhat,
lbruhat@stanford.edu

Citation:
Bruhat L., and P. Segall (2016), Coupling on the northern Cascadia subduction zone from geodetic measurements and physics-based models, *J. Geophys. Res. Solid Earth*, *121*, doi:10.1002/2016JB013267.

Received 11 JUN 2016
Accepted 23 OCT 2016
Accepted article online 27 OCT 2016

Abstract Kinematic inversions of GPS and tide gauge/leveling data display an unresolved "gap" between the downdip limit of the locked megathrust and the top of the episodic tremor and slip (ETS) zone in northern Cascadia. This work combines physics-based models of slow-slip events with both mean ETS displacements and decadal-averaged deformation rates to explain the gap and determine how interseismic stress accumulates on the megathrust. While physics-based predictions match the average ETS displacements, they significantly misfit long-term rates, implying faster slip rates within both the gap and the ETS region. Heterogeneous Green's functions or velocity-strengthening friction within the gap cannot explain the decadal rates. The observed uplift rates require steeper gradients in slip rate at the base of the locked zone. We invert for the smallest possible shear stress rate on the creeping megathrust below a locked zone that satisfactorily fits the data. A nonzero shear stress rate within the ETS zone, reaching −2.5 kPa/yr at a depth of 25–30 km, is required. Finally, of all the models that adequately fit both horizontal and vertical data, only those with deep locking depths, around 21 km, significantly improve the fit to the uplift rates.

1. Introduction

The Cascadia subduction zone, where the Juan de Fuca plate subducts beneath North America, presents one of the greatest earthquake hazards in the U.S. Due to the lack of historical data, little is known about the last megathrust event, an approximately magnitude 9 earthquake that occurred in January 1700 [*Satake et al.*, 1996; *Satake*, 2003]. Because of the absence of direct coseismic observations, efforts to assess the seismic hazard are concentrated on estimating recurrence intervals of large earthquakes, using onshore and marine paleoseismic records [*Atwater*, 1987; *Atwater et al.*, 1995; *Satake et al.*, 1996; *Goldfinger et al.*, 2003], and on evaluating where and how fast strain accumulates along the plate interface [*Mitchell et al.*, 1994; *Hyndman and Wang*, 1995; *Flück et al.*, 1997; *McCaffrey et al.*, 2007; *Burgette et al.*, 2009; *Holtkamp and Brudzinski*, 2010; *Krogstad et al.*, 2016]. In particular, one of the key unknowns remains the downdip depth extent of the locked megathrust, which is important because a deeper rupture implies greater coseismic slip near major population centers such as Seattle, Vancouver, and Portland.

An upper bound on the downdip extent of the locked region has been suggested by the presence of intermittent aseismic slip episodes, called slow-slip events (SSEs) [*Hyndman*, 2013]. Evidence for slow slip on the Cascadia subduction zone was first described by *Dragert* [2001], after recording brief, episodic reversals in continuous GPS position time series. *Dragert* [2001] interpreted these signals as resulting from magnitude 6.7 events with ~2 cm of slip over a period of 1 to 2 weeks. SSEs are accompanied by tremors, thought to be composed of low-amplitude, low-frequency earthquakes [*Rogers and Dragert*, 2003; *Dragert et al.*, 2004; *Dragert and Wang*, 2011; *Ghosh et al.*, 2012]. This phenomenon, also known as episodic tremor and slip (ETS), has been observed in other subduction zones such as Japan [*Heki et al.*, 1997] and Mexico [*Lowry et al.*, 2001].

In northern Cascadia, SSEs occur approximately every 15 months [*Szeliga*, 2004; *Brudzinski and Allen*, 2007] lasting a few days to a few weeks and yielding 2 to 5 cm of slip [*Dragert et al.*, 2004; *Schmidt and Gao*, 2010; *Bartlow et al.*, 2011]. Tremor migrates along strike at a rate of roughly 10 km/d [*Dragert et al.*, 2004; *Wech et al.*, 2009; *Dragert and Wang*, 2011]. In this region, locations and timing of tremors and geodetic inversions of slow slip reveal that these two phenomena are closely linked [*Bartlow et al.*, 2011; *Hawthorne and Rubin*, 2013; *Wech and Bartlow*, 2014]. The spatial distribution of tremors has thus been used to infer the distribution of slow slip (Figure 1). ETS events are concentrated at depths between 25–30 km and 50 km [*Wech et al.*, 2009;

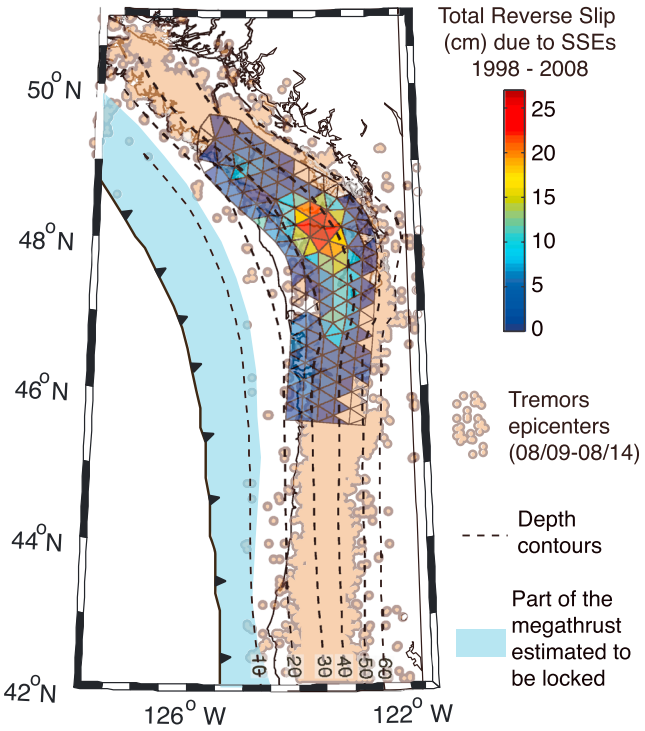

Figure 1. Locking model and locations of tremor and slow-slip events (SSEs). Colored dots are the locations of tremor epicenters from August 2009 to August 2014 from *Wech* [2010]. The locking depth of the megathrust estimated at ≈12 km by *Burgette et al.* [2009] in northern Cascadia is shown. The distribution of cumulative slip due to slow-slip events from 1998 to 2008 [*Schmidt and Gao*, 2010]. Depth contours on the plate interface model of *McCrory et al.* [2012].

Holtkamp and Brudzinski, 2010; *Bartlow et al.*, 2011; *Wech and Bartlow*, 2014], depending in part on which plate boundary model is employed [e.g., *McCrory et al.*, 2012].

Observations from the Nankai region in Japan [*Obara*, 2011] suggest that the updip limit of ETS corresponds to the downdip extent of previous *M* 8 earthquakes. However, in Cascadia, geodetic measurements have been interpreted to conclude that the megathrust is fully locked to a depth of only 10–17 km [*Hyndman and Wang*, 1995; *Flück et al.*, 1997; *McCaffrey et al.*, 2007; *Burgette et al.*, 2009], leading to an enigmatic "gap" between the locked region and top of the ETS zone [*Dragert et al.*, 2004; *McCaffrey et al.*, 2007; *Wech and Creager*, 2011; *McCaffrey et al.*, 2013; *Hyndman*, 2013]. The gap complicates estimations of the depth extent of future megathrust earthquakes, which might propagate downdip either to the end of the fully locked region at 10–17 km or to the top of the ETS zone at 25–30 km, placing the rupture zone closer to large cities, such as Seattle or Portland. Since the magnitude of an earthquake increases with rupture area, it is critical to address the current state of this gap and to determine whether seismic rupture would propagate into this region.

Numerical physics-based models have the potential to shed light on this problem. *Segall and Bradley*, 2010 [2010, 2012a] developed 2-D quasi-dynamic simulations of the complete seismic cycle in a subduction setting like Cascadia. The focus of this work was to understand the depth distribution of physical properties that could explain SSE. They successfully reproduced qualitative features of SSE between 25 km and 50 km depth, interrupted every several centuries by large megathrust events that rupture the updip locked region. Their model employed rate and state friction, dilatancy for stabilizing slow-slip events, and thermal pressurization during fast slip. As slip nucleates in the ETS region, dilatancy causes the pore volume to increase, deceasing pore pressure, thus increasing the effective normal stress and therefore the frictional resistance to further slip. In these models the shear stress within the SSE zone, when averaged over many SSE cycles, remains roughly constant; stress builds up between SSEs but is then released during SSE slip.

In the *Segall and Bradley* [2012a] simulations the megathrust was locked interseismically down to the ETS region, i.e., there was no gap. In one class of solutions SSEs are trapped in a region of low effective normal stress, which gradually builds a stress concentration at the border of the locked region and the SSE zone. Ultimately, a SSE becomes unstable and triggers rupture of the updip, locked region. In these simulations there do not appear to be observable differences between the preceding SSE and the one that ultimately generates a model megathrust event. All solutions produced dynamic events that propagate both updip and downdip into the ETS region, in contrast with interpretations of the Nankai data, discussed above. Strong dilatancy within the ETS zone could prevent dynamic ruptures from propagating into the ETS region [*Segall and Bradley*, 2012a; *Liu*, 2013], although that slip would ultimately be accommodated through afterslip.

Little is known about the nature, and even about the existence, of the gap between the locked zone and the top of the ETS zone. If creep occurs in the gap, it would have important implications for the mechanical

relationship between deep slow-slip and dynamic events on the seismogenic part of the fault. In this study, we analyze average ETS displacements and deformation rates in the Olympic Peninsula-southern Vancouver Island region to determine how much interseismic strain accumulates on the megathrust. In particular, we focus on understanding the nature of the putative gap between the top of the ETS zone and the bottom of the interseismic locked zone.

We first apply the physics-based models developed by *Segall and Bradley* [2012a] to the Cascadia subduction zone, with the intention of fitting both the average ETS displacements and the decadal-averaged geodetic velocities. Although model predictions can match the ETS displacements, they fail to fit observed decadal-scale velocities, in particular the uplift rates from a combination of leveling and tide gauge data, when the fault is locked to the top of the ETS zone. To better understand this issue, we first consider the potential bias caused by the use of homogeneous Green's functions to relate the slip on the megathrust to the surface displacements, compared to more realistic Green's functions that assume a stiff oceanic slab. We also test a common suggestion that the gap is creeping steadily [*Holtkamp and Brudzinski*, 2010; *Hyndman*, 2013; *Schmalzle et al.*, 2014]. For that we modify the physics-based models, including creeping zones at the top of the ETS region, to explain the inferred slip in both the gap and ETS region.

We find that the misfit between observations and predictions from physics-based simulations with creep in the gap persists, leading us to develop a new approach to assess the mechanical behavior of the ETS region and to construct more accurate physics-based models. Specifically, we invert for shear stress rates on the megathrust that best fits the data. Using this approach, we show that the deformation data can be explained by negative shear stress rates, up to 2.5 kPa/yr, at the top of the ETS region. This small change in shear stress on the megathrust is sufficient to produce steeper slip rate gradients at the updip limit of the ETS region. We also demonstrate that among the models that fit the entire data set, only those with locking depths to ~21 km are able to fit to the observed uplift rates.

2. Numerical Simulations of Slow-Slip and Dynamic Rupture Applied to Cascadia

2.1. Geodetic Observations

Observations of deformation rates in the Olympic Peninsula-southern Vancouver Island region include (1) displacements and velocities obtained from GPS measurements and (2) uplift rates, determined from tide gauges and leveling measurements. We focus on this region because of the abundance of data and minimal fore-arc rotation. Since the physics-based models are one dimensional (with depth) we prefer avoiding strain partitioning generated by oblique convergence.

We use daily GPS positions at 51 stations from PANGA, the Pacific Northwest Geodetic Array, Central Washington University (http://www.geodesy.cwu.edu/data/bysite/), from 2000 to mid-2015, from which we compute horizontal velocities averaged over numerous past SSEs and uncertainties assuming 1 mm of white noise and random walk of 1 mm/yr$^{0.5}$ (Table S1 in the supporting information). We refer to these decadal-averaged rates as "long term." The locations of the GPS stations are displayed in Figure 2a. Uncertainties in the vertical component are based on 3 mm white noise and a random walk scale of 1 mm/yr$^{0.5}$ [*Dmitrieva and Segall*, 2015]. We do not consider the GPS vertical velocities in this study because of the large uncertainties.

We also compute the average ETS displacements from the GPS positions. We consider eight ETS events from December 2000 to December 2014. The times of the ETS events come from tremor logs [*Schmidt and Gao*, 2010] (and after 2008, http://www.pnsn.org/tremor/overview). We fit the GPS time series with a sawtooth model which assumes constant inter-SSE rate but variable displacement during ETS events. We then compute the mean ETS displacement. Figure 2c displays the estimated linear trends, inter-SSE, and ETS displacements for four sample GPS time series. The resulting ETS displacements and horizontal long-term rates are presented in Figure 3.

We also employ uplift rates from tide gauges and leveling surveys in the northern Washington area along the Strait of Juan de Fuca and on the east side of the Puget Sound from *Krogstad et al.* [2016] (Figures 2 and 3 and Table S2). These rates assume zero vertical motion at the Seattle tide gauge, consistent with regional sea level reconstructions [*Burgette et al.*, 2009]. To account for the possibility that this assumption is incorrect, we include a free parameter in the inversions that allow the vertical rates to shift uniformly. *James et al.* [2009] provided predictions of present-day uplift rates due to postglacial rebound, ranging from ~0.35 mm/yr to ~0.5 mm/yr. We correct the uplift rates from *Krogstad et al.* [2016] by removing the predictions of *James et al.* [2009].

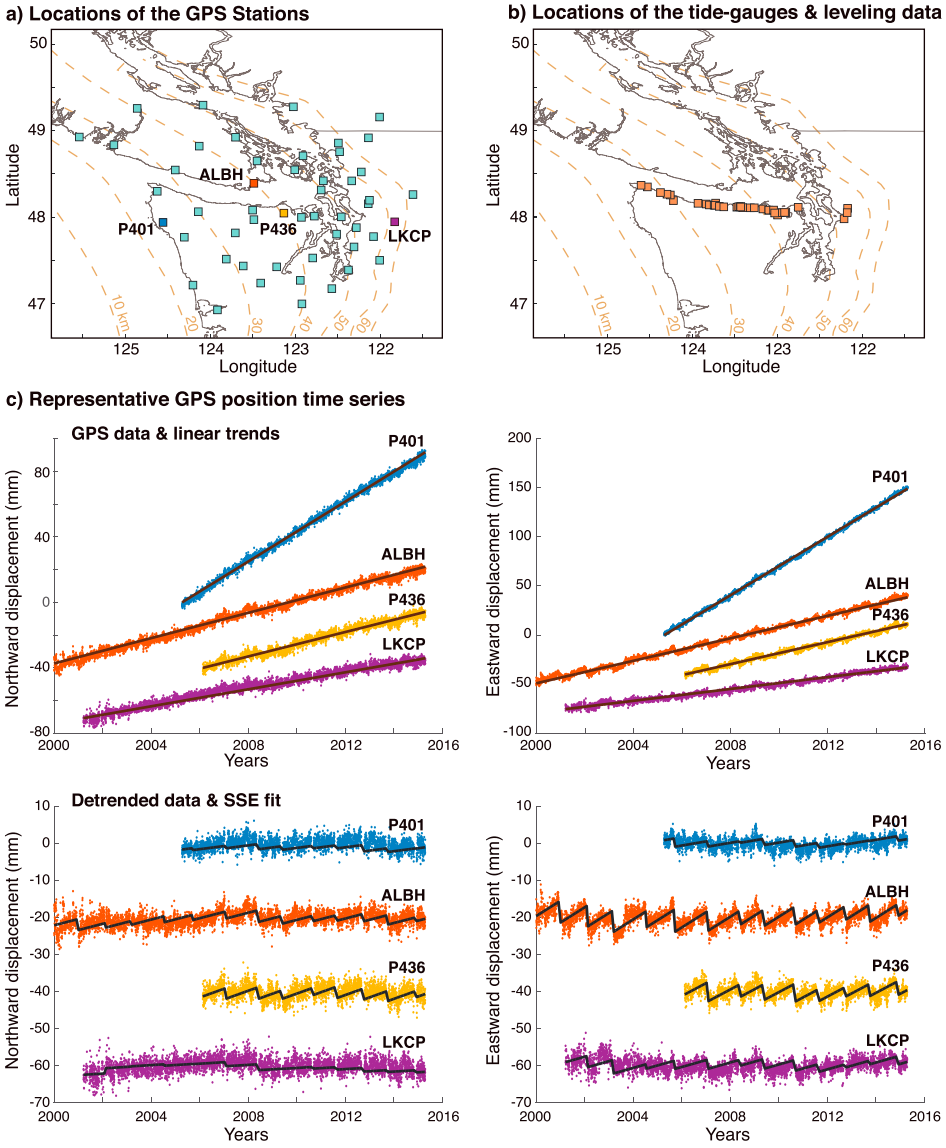

Figure 2. Description of the data used in this study. (a) Locations of the 51 GPS stations. (b) Location of the tide gauges and leveling measurements. (c) Time series of four representative GPS stations, showing the north and east displacements and the inverted long-term velocity and SSE fit.

2.2. Predictions of ETS Displacements and Long-Term Slip Rates

Segall and Bradley [2010; 2012a] developed numerical methods that produce both slow-slip events and dynamic events on the megathrust. In this section, we apply these physics-based models to the average ETS displacements and long-term rates in northern Cascadia.

We use FDRA (Fault Dynamics Radiation-damping Approximation), a quasi-dynamic BEM (Boundary Element Method) code for faults with rate and state friction in poro-thermo diffusive elastic half-spaces [*Segall and Bradley*, 2010, 2012a, 2012b]. Slip is in the x direction, and the deformation is plane strain (Figure 4). In this part of the study, we only simulate the ETS region between 30 and 42 km for computational efficiency. As a consequence, the part of the fault between the trench and 30 km is assumed to be locked. Below 42 km, we impose slip at the plate velocity of 37 mm/yr.

The distributions of effective normal stress $\bar{\sigma} \equiv \sigma - p$, where σ is fault normal stress and p pore pressure, and frictional properties are similar to *Segall and Bradley* [2012a] (Figure 4). As shown by *Audet et al.* [2009] and *Audet and Bürgmann* [2014], ETS regions are characterized by very low effective normal stresses. We set $\bar{\sigma}$ to be 1 MPa inside the ETS region and of the order of 12 MPa at shallower depth. Downdip of the ETS region,

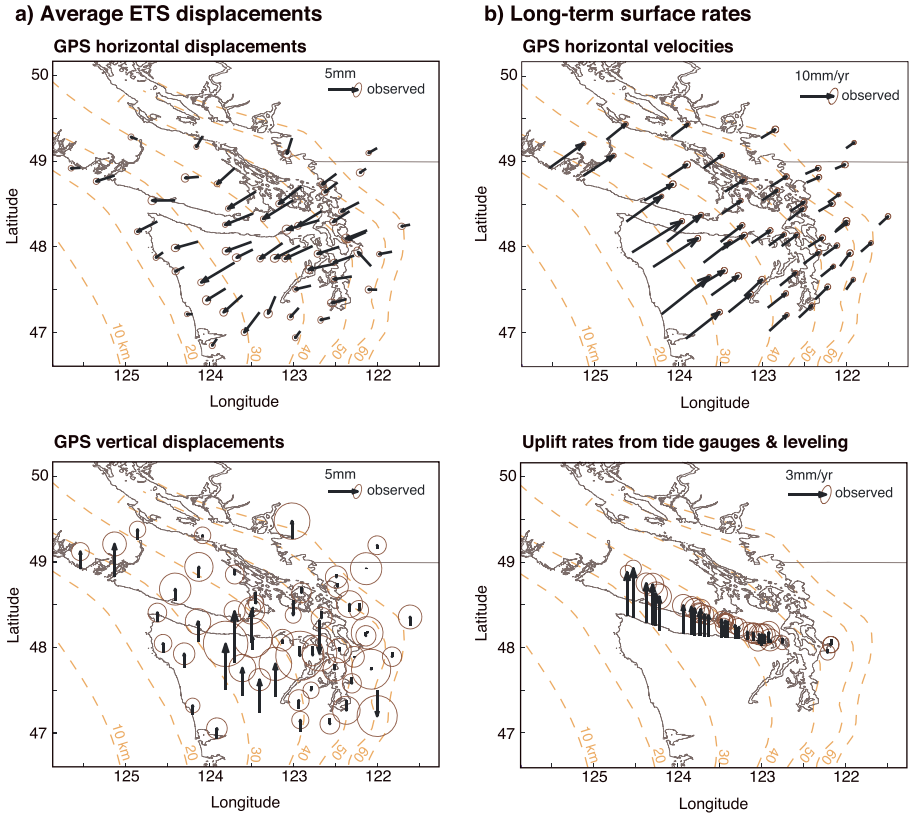

Figure 3. Data set used in this study. (a) Horizontal and vertical ETS displacements averaged over eight ETS events from 2000 to May 2015, computed from the GPS time series. (b) Decadal-averaged, in this study called long-term, surface rates. Horizontal GPS velocities directly computed from the daily positions (top row). Uplift rates from *Krogstad et al.* [2016], corrected for postglacial rebound (bottom row). Uncertainties correspond to the 95% confidence interval.

$\bar{\sigma}$ transitions to 110 MPa. The simulations use a rate and state friction law, assuming the aging law for state evolution. The depth distribution of frictional properties roughly follows *Liu and Rice* [2009]: the coefficient a increases as a function of the temperature T, as $a = \lambda(T + 273.15)$, where $\lambda = 3.5 \times 10^5$/°C and T follows the geotherm given by *Peacock* [2009]. The coefficient for state evolution b is calculated such that $a - b = -0.0035$ in the velocity-weakening region, and $a - b$ increases linearly below ~34 km (loosely following *He et al.* [2007]),

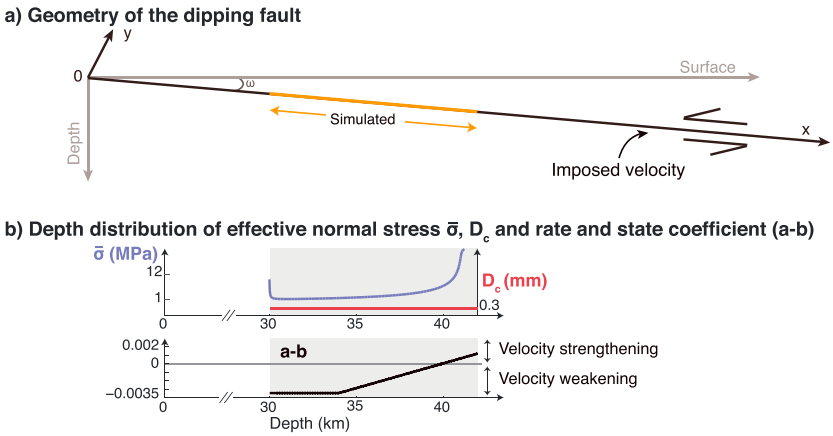

Figure 4. (a) Geometry of the dipping fault adapted from *Segall and Bradley* [2012a]. Imposed plate motion velocity is equal to 37 mm/yr in northern Cascadia. We only simulate the ETS region between 30 and 42 km. (b) Depth distribution of effective normal stress $\bar{\sigma}$, critical slip-weakening distance D_c, and steady state velocity dependence coefficient (Figures 4a and 4b).

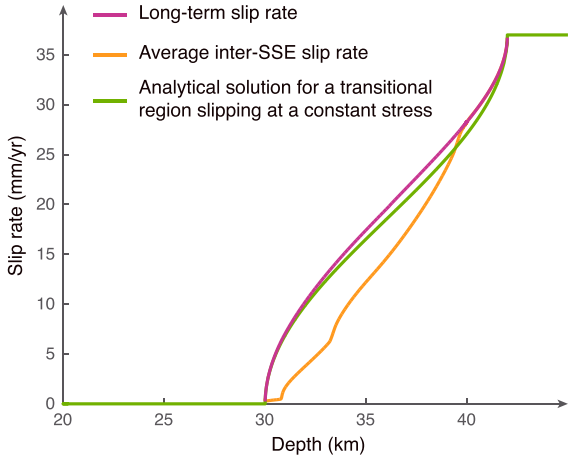

Figure 5. Long-term slip rate profile computed from the physics-based ETS numerical models applied to northern Cascadia. The numerical result is very close to the solution for a transition region slipping at a constant resistive stress, between locked and specified slip rate zones [*Segall*, 2010, section 12.1].

becoming positive at depths below 40 km. The critical slip-weakening distance D_c is 0.3 mm at all depths. These parameter choices do not uniquely or even properly represent the megathrust interface; rather, they are chosen to illustrate a particular class of model behavior.

Unlike *Segall and Bradley* [2012a], slow-slip events here are simulated using isothermal v-cutoff models, as developed by *Shibazaki and Shimamoto* [2007]. This approach limits computational time and is qualitatively similar to models with dilatant strengthening. These models posit a limiting slip speed, called the cutoff velocity, that allows slow-slip events to occur. We employ the form of the rate and state friction law with cutoff velocities, proposed by *Okubo* [1989] and *Brechet and Estrin* [1994], where the coefficient of friction μ is related to the slip speed v, the state variable θ, and two cutoff velocities v_1 and v_2 through

$$\mu = \mu_* - a \log\left(\frac{v_1}{v} + 1\right) + b \log\left(\frac{v_2 \theta}{D_c} + 1\right) \tag{1}$$

Following *Shibazaki and Shimamoto* [2007], we impose $v_1 = 1$ m/s, in order to limit the slip speed during model SSE by changing v_2 only. The cutoff velocity v_2 is chosen to be 10^{-7} m/s or 8.6 mm/d, consistent with observed slip rates for ETS events in northern Cascadia. The state variable θ describes the average contact time of the asperities on the sliding surface. The aging law form of state evolution is employed [*Ruina*, 1983], and v_2 is kept constant within the ETS region.

The modeled long-term slip rate profile, averaged over numerous model SSEs, is presented in Figure 5. The fault is locked to a depth of 30 km leading to a steep increase in slip rate in the upper part of the ETS region. We also display the analytical solution for a region slipping at constant stress between a locked zone and a deep imposed-velocity boundary [e.g., *Segall*, 2010, section 12.1]. As noted by *Segall and Bradley* [2012a] the fact that the analytical and numerical profiles are so similar indicates that shear stress in the ETS region builds up between SSEs, but is then released during events, such that the stress stays roughly constant over the long term.

Since these FDRA calculations are two dimensional, we adopt a pseudo 3-D approach to compare model predictions with data. FDRA produces one-dimensional, along-fault profiles of both average ETS slip and long-term slip rate. These 1-D profiles are repeated along strike and draped over the plate boundary geometry from *McCrory et al.* [2012]. For every point on the plate boundary we assign slip (or slip rate) based on the depth of that point from the 1-D numerical results. This yields a 2-D slip rate distribution, which allows us to predict deformation rates at the Earth's surface, but does not account for along-strike heterogeneity or slip variations due to nonplanarity of the plate boundary. For the average ETS displacement only, the 1-D slip profile is also smoothed along strike to limit the length of the ETS region to 300 km along strike. If y is the distance between the evaluation point and the reference line of the ETS slip profile, then the smoothing factor is $(1 - y^2)^{1.5}$ on both sides of this reference line. To estimate the along-strike length of ETS slip, we invert the average ETS displacements for slip distribution between 30 and 42 km depth (Figure S1). While this tapering is ad hoc, it does permit us to compare 2-D numerical simulations with geodetic data.

Predicted ETS slip and long-term slip rate distributions are displayed in Figures 6a and 6b. This model, which assumes a locked plate boundary between 0 and 30 km, an ETS region between 30 and 42 km, and an imposed downdip velocity below 42 km, fits the average ETS displacements reasonably well, especially for the

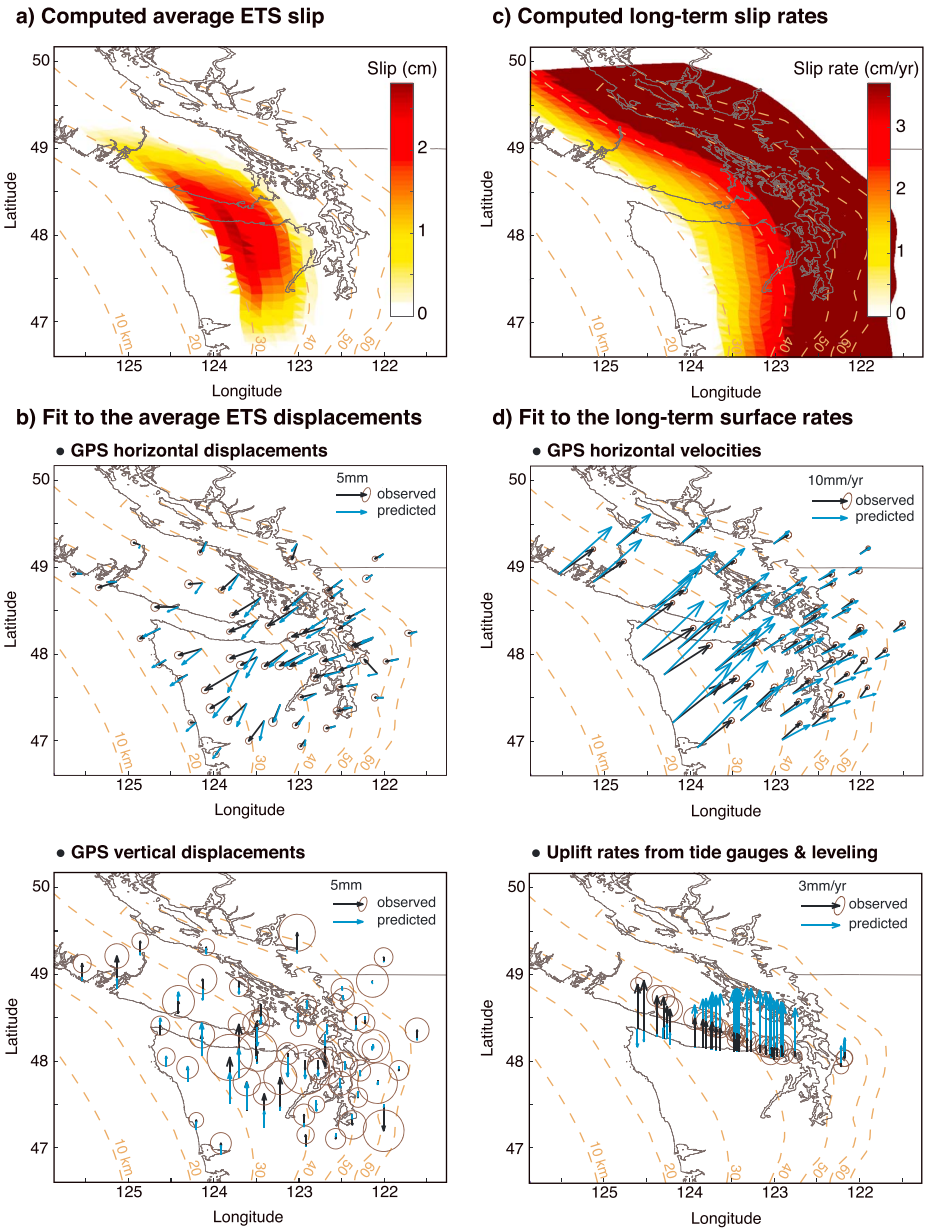

Figure 6. (a) Computed average ETS displacement, (c) long-term slip rates, and (b and d) their corresponding fit to the surface data. VR stands for variance reduction. Numerical simulations consider a fully locked region between 0 and 30 km and an ETS zone spanning 30–42 km depth. Our physics-based predictions fit the average ETS event within the uncertainties but fail at matching the long-term rates, particularly the uplift rates.

horizontal component (Figure 6b). In addition, 76% of the predicted vertical displacements match the sign of the GPS observations. However, this model overpredicts the horizontal long-term velocity in the western part of the network (Figure 6d). The misfit indicates too much locking between 15 and 30 km, in other words, in "the gap" defined previously. Similarly, the forward model completely fails at fitting the long-term uplift rates.

This section presented physics-based models which match the ETS average displacements reasonably well and suggest that the ETS acts as constant stress transition zone, as seen in Figure 5. However, the physics-based model fails at fitting the long-term rates, especially the vertical rates. In the rest of this study we investigate solutions to explain this discrepancy.

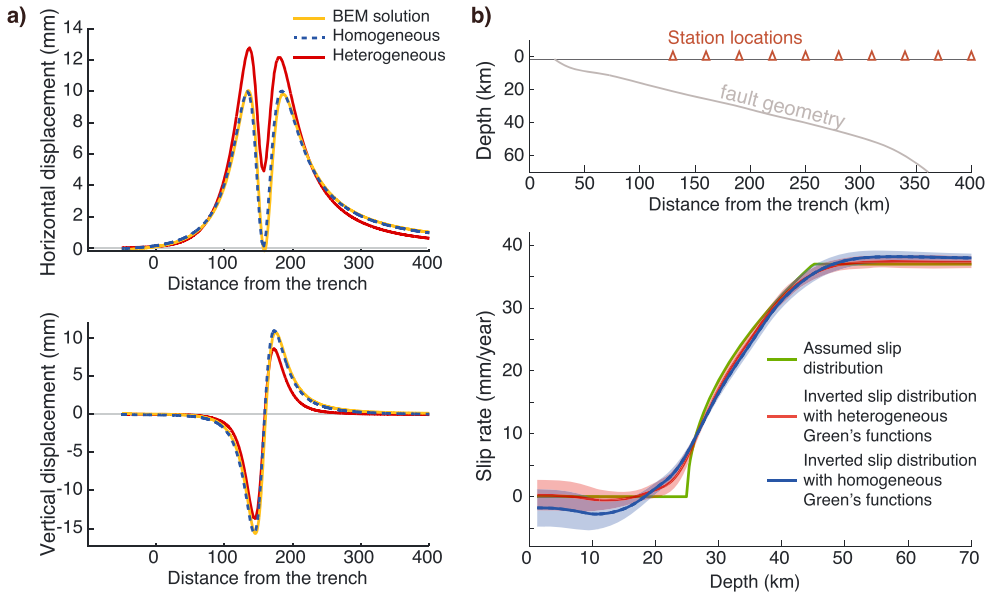

Figure 7. Effect of heterogeneous Green's functions on the slip rate inversions. (a) Surface displacements caused by 1 m of back (normal) slip at 25 km of depth computed using three different Green's functions. The blue dashed and red solid lines are the surface displacements from, respectively, homogeneous and heterogeneous Green's functions computed using the FEM code PyLith. The yellow lines are from analytical solution for a homogeneous half-space. (b) Comparison between synthetic inversions using homogeneous and heterogeneous Green's functions. The heterogeneous Green's functions are computed considering an extreme value for the oceanic mantle shear modulus.

3. Explaining Long-Term Rates With Physics-Based Models

3.1. Evaluation of Potential Effects of Crust-Mantle Structure

The discrepancy between the long-term observations, especially the vertical rates, and the predicted rates from physics-based models could potentially be caused by inaccurate Green's functions. Most previous analyses assume a homogeneous half-space, but the presence of a relatively stiff subducting slab can bias the surface velocity distribution. To address this issue, we compute Green's functions for a heterogeneous half-space using PyLith [*Aagaard et al.*, 2013], a finite-element code for dynamic and quasi-static simulations of crustal deformation, developed by the Computational Infrastructure for Geodynamics.

We construct a 2-D mesh composed of triangular cells using the mesher CUBIT. The fault geometry is inferred from the plate interface model of *McCrory et al.* [2012]. We divide the mesh into fours blocks: the oceanic mantle, the oceanic crust, the continental crust, and the continental mantle. To validate the numerical results, we compare the surface displacements caused by 1 m of back slip at 25 km depth in a homogeneous medium obtained from PyLith with those predicted by analytical Green's functions in a homogeneous half-space in Figure 7a. We find a very good agreement; the differences between methods in homogeneous medium are small compared to the influence of the heterogeneous properties.

Hu and Wang [2012] set the shear moduli to 48 GPa in the continental and the oceanic crust and 64 GPa in the continental and the oceanic mantle. Ignoring this contrast between the shear moduli in the oceanic crust and mantle might bias the inverted slip rate distribution. Because the modulus contrast can be greater at quasi-static as opposed to seismic frequencies, we test an extreme value of 192 GPa (3×64 GPa) for the oceanic mantle. The surface displacements caused by 1 m of back slip at 25 km depth in this heterogeneous medium are displayed in Figure 7a. We then test the effect of the heterogeneous Green's functions the following way. We first assume a slip rate distribution where the megathrust is locked above 25 km, an assumed slip rate profile between 25 and 50 km depth, with constant slip rate below 50 km, from which we compute synthetic horizontal and vertical displacements at 10 inland stations, using the *heterogeneous* Green's functions. We perturb the synthetic data, by adding 0.5 mm/yr of white noise, then invert the data using the *homogeneous* Green's functions. This approximates what might happen by using homogeneous Green's functions to invert data from a realistic Earth. The inversion solves the following least squares problem:

$$\min ||\mathbf{G}_{\text{homog}}\dot{\mathbf{s}} - \mathbf{d}_{\text{syn}}||_2^2 + \alpha^2||\mathbf{L}\dot{\mathbf{s}}||_2^2 \quad (2)$$

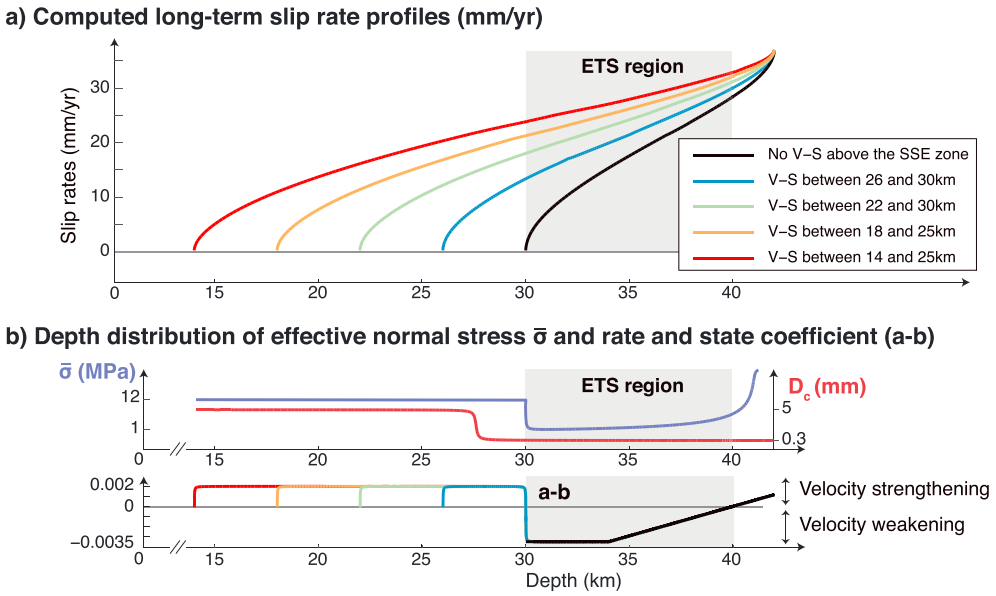

Figure 8. (a) Predicted slip rate profiles with various-sized velocity-strengthening (V-S) regions updip of the ETS zone. (b) Depth distribution of effective normal stress $\bar{\sigma}$, critical distance D_c, and rate and state coefficients (a-b).

where $\mathbf{G}_{homog}$ are the homogeneous Green's functions, $\dot{\mathbf{s}}$ is the unknown slip rate distribution, $\mathbf{d}_{syn}$ the perturbed synthetic data, α the regularization parameter, and $\mathbf{L}$ the finite-difference operator for the first derivative. We choose an α such that we fit the synthetic data within the 95% confidence interval but exclude overly rough solutions. Finally, we conduct the same inversion using the heterogeneous Green's functions. The two inversions are repeated 500 times for different perturbed synthetic horizontal and vertical data. The inverted slip distributions are compared in Figure 7b with the one standard deviation uncertainty indicated by the corresponding shaded region. Using heterogeneous Green's functions results in slightly less slip above 25 km, but the difference is small and insufficient to account for the gap between the bottom of the locked zone and the top ETS region. We conclude that biased Green's functions are unlikely to explain the gap.

3.2. Can the Gap be Explained by Creep at Constant Stress?

Having established that the use of homogeneous Green's functions is unlikely to explain the discrepancy between the estimated downdip limit of the locked region and the location of slow-slip events, we now investigate physical mechanisms that could explain why the long-term deformation rates seem to require less locking updip of the SSE region. One possibility is that creep updip of the ETS zone results from velocity-strengthening rheology, which allows the gap to creep at constant stress. This has previously been proposed as a possible explanation for the gap [*Holtkamp and Brudzinski*, 2010; *Hyndman*, 2013; *Schmalzle et al.*, 2014]. We test this hypothesis through numerical models that include velocity-strengthening regions updip of the ETS region, from which we compute predicted long-term velocities.

We return to the numerical simulations described in the previous section. Creep at constant stress can be induced by adding a velocity-strengthening region within the gap. In these calculations we expand the size of the fault updip, accounting for velocity-strengthening regions of different lengths at the top of the ETS zone that is above 30 km. The ETS region is still defined between 30 and 40 km. Within the ETS region, we use the same effective normal stress $\bar{\sigma}$, critical slip-weakening distance D_c, and rate and state coefficients (a, b) as described previously (Figure 8b). The transition to larger D_c is moved a few kilometers updip of the transition in effective normal stress.

We test four lengths of the velocity-strengthening region, with updip extent from 26 km to 14 km depth. As described previously, we only simulate the region between the upper end of the velocity-strengthening region and 42 km. The shallower region is constrained to be locked. The computed long-term slip rates for each simulation are displayed in Figure 8a. The profiles again correspond very closely to the slip rate profile for a transitional region slipping at constant resistive stress [e.g., *Segall*, 2010, section 12.1]. The addition of a shallow velocity-strengthening region, which over the long-term slips at constant stress, extends

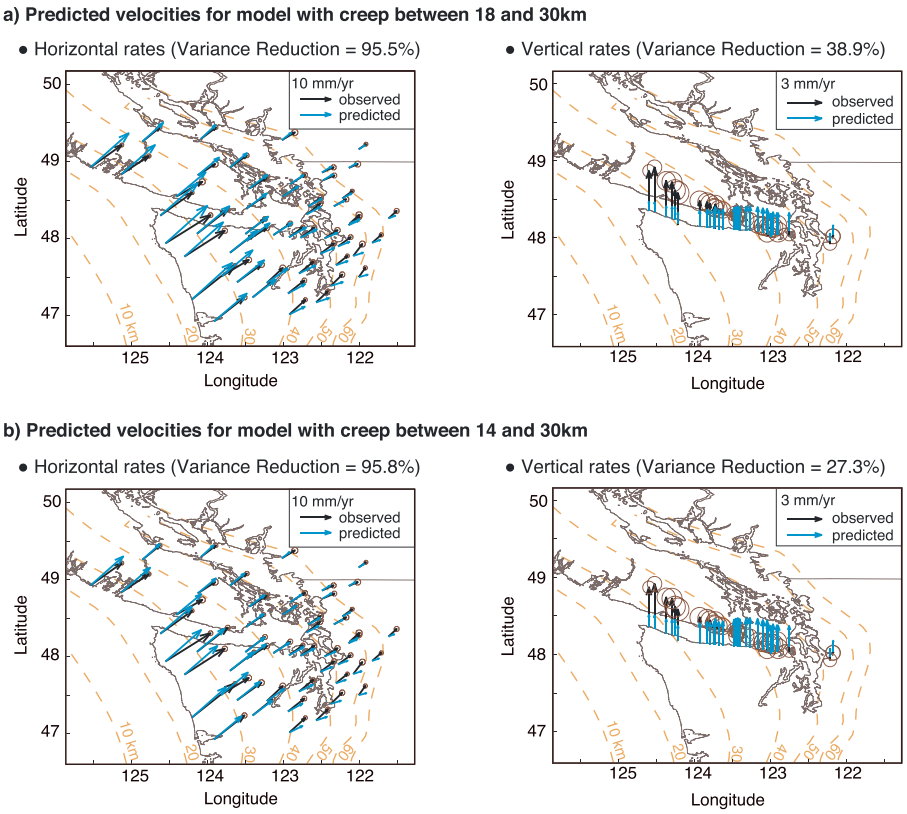

Figure 9. (a, b) Predicted and observed vertical and horizontal rates for two slip rate profiles with velocity-strengthening regions updip of the ETS zone. Larger velocity-strengthening regions improve the fit to the horizontal velocities (left column). However, these models fail at fitting the uplift rates (right column).

the length of the crack, explaining the similarity between the slip rate profiles computed with and without velocity-strengthening zone updip of the ETS region.

Using these four slip rate profiles, we compute the predicted surface deformation rates $\mathbf{d}_{\text{pred}}$ to compare with observed velocities. Figure 9 shows that with creep in the gap the predicted surface deformation rates $\mathbf{d}_{\text{pred}}$ improve the fit to the horizontal displacements; however, they still severely misfit the vertical rates. These results show that a creeping region at constant stress at the top of the ETS region does not alone provide a sufficient explanation for the high uplift rates on the Olympic Peninsula.

As a way to understand what the data require, in terms of the smallest perturbation to the a priori physical models, we invert the residuals $\mathbf{r} = \mathbf{d}_{\text{pred}} - \mathbf{d}_{\text{obs}}$ from the five starting physics-based models, attempting to find plausible fits to both the vertical and horizontal rates. For that, we solve the following regularized inverse problem:

$$\min ||\boldsymbol{\Sigma}^{-1/2}(\mathbf{G}\dot{\mathbf{s}}_{\text{corr}} - \mathbf{r})||_2^2 + \alpha^2 ||\dot{\mathbf{s}}_{\text{corr}}||_2^2 \tag{3}$$

where $\boldsymbol{\Sigma}$ is the data covariance matrix, $\mathbf{G}$ the homogeneous Green's functions, $\dot{\mathbf{s}}_{\text{corr}}$ is the unknown slip rate correction, and α the regularization parameter, which is qualitatively chosen to get a good fit within the uncertainties avoiding an overly rough solution. The inferred correction is then added to the starting slip rate distribution. Note that the minimum norm regularization ensures that we find the smallest perturbations to the a priori physical models that fit the data within errors. The regularization parameter α is the same for all starting models.

The adjusted slip rate distribution is displayed in Figure 10a. Not surprisingly, all the starting models converge to similar slip rate distributions. These models all exhibit shallow creep (≈10 to 15 mm/yr), in a region between 15 and 25 km and slip rates in excess of those predicted by constant stress models below 25 km. The transition near 25 km is characterized by a steep increase in slip rates, from nearly 10–15 mm/yr to

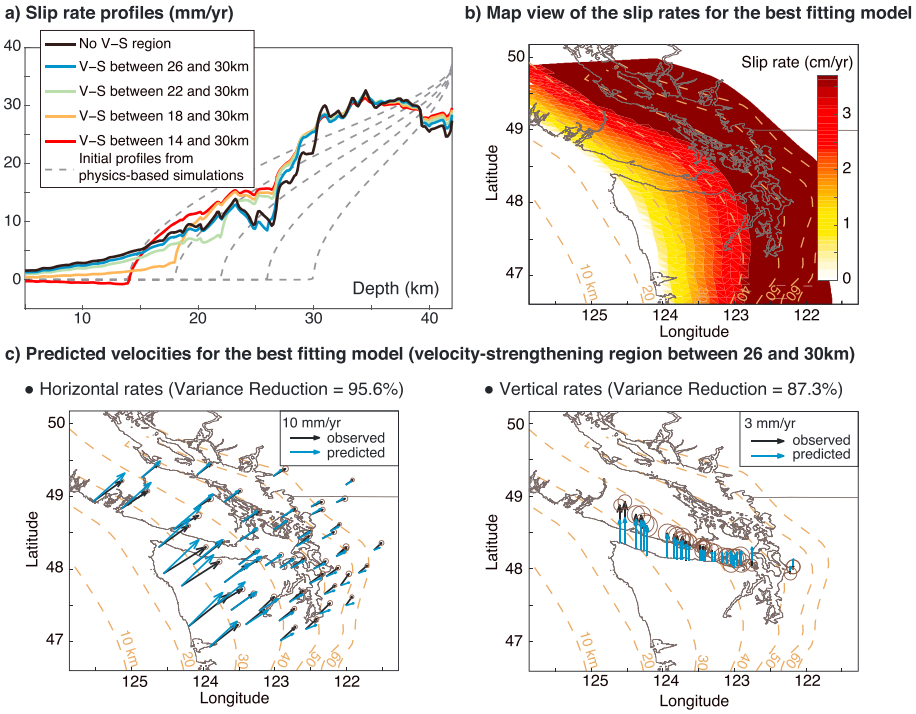

Figure 10. Inverted slip distributions, which fit both the horizontal and vertical rates. (a) Grey dashed curves show forward slip rate predictions with various-sized velocity-strengthening zones updip of the ETS zone. Colored curves show slip rates adjusted to fit GPS and uplift data. (b) Map view of the slip rate distribution for the best fitting model, with a velocity-strengthening region between 26 and 30 km. (c) Predicted and observed vertical and horizontal rates for the best fitting model.

~30 mm/yr. This sharp rise in slip rates is necessary to fit the high uplift rates along the Juan de Fuca Strait. Below ~30 km depth, slip rates converge gradually toward the plate velocity. Relative to the predicted surface deformation rates from the starting (constant stress) models, the fit to the data has improved for both the horizontal and vertical components. However, the models still underpredict uplift rates at stations on the western end of the Olympic Peninsula and overpredict uplift rates at the easternmost stations. So although a velocity-strengthening region above the ETS zone allows creep in the gap, creep at constant stress predicts neither the sharp gradient in slip rate nor the high slip rates between 25 and 40 km depth required to fit the uplift data.

4. Inversion for Shear Stress Rates

Having shown that a velocity-strengthening region updip of the ETS region cannot adequately fit observed uplift rates and that faster slip rates between 25 and 45 km are necessary, we investigate physically motivated models that could explain such a slip rate profile. For the fault to slip faster between 25 and 45 km, the shear stress must decrease with time in this region. Note that this conflicts with the conclusions of the a priori physics-based models that, when averaged over many SSE cycles, that shear stress within the SSE zone remains roughly constant over time. Consequently, as an intermediate step between kinematic inversions and fully physics-based predictions we invert the long-term data for shear stress rates on the megathrust.

Standard approaches invert surface velocities $\mathbf{d}$ for fault slip rates $\dot{\mathbf{s}}$

$$\mathbf{d} = \mathbf{G}\dot{\mathbf{s}} + \epsilon \quad \text{with} \quad \epsilon \sim \mathcal{N}(0, \boldsymbol{\Sigma}) \tag{4}$$

The stressing rate on the fault is also related to the slip rate through elastic Green's functions of the form

$$\dot{\boldsymbol{\tau}} = \mathbf{A}\dot{\mathbf{s}} \tag{5}$$

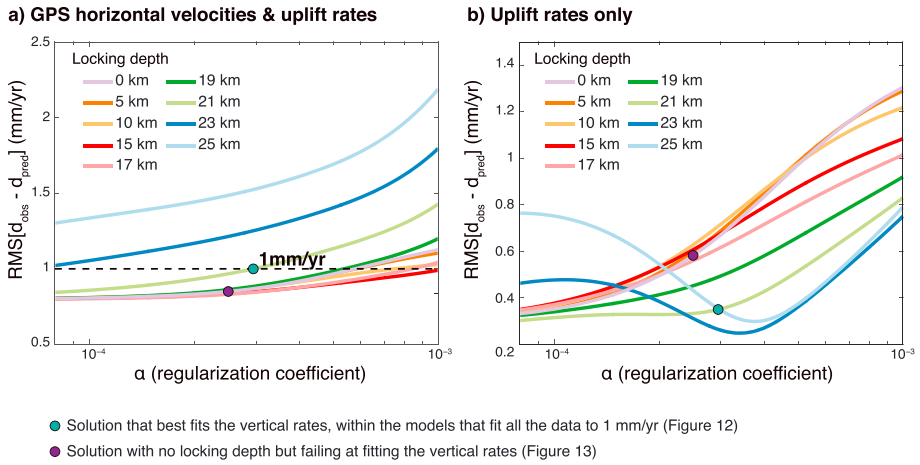

Figure 11. Root-mean-square of the residuals of the (a) entire data set and (b) vertical rates only as a function of the regularization parameter α for each considered locking depth. Among the models that fit all the data within 1 mm/yr, only the one with the 21 km locking depth best fits the uplift rates (green filled circle). The solution presented in Figure 13, without imposed locking depth, is indicated by the purple filled circle.

Combining (4) and (5) gives

$$\mathbf{d} = \mathbf{G}\mathbf{A}^{-1}\dot{\boldsymbol{\tau}} + \epsilon \tag{6}$$

We then estimate $\dot{\boldsymbol{\tau}}$ by solving this new regularized least squares problem

$$\min ||\boldsymbol{\Sigma}^{-1/2}\left(\mathbf{G}\mathbf{A}^{-1}\dot{\boldsymbol{\tau}} - \mathbf{d}\right)||_2^2 + \alpha^2||\dot{\boldsymbol{\tau}}||_2^2 \tag{7}$$

Note that the regularization seeks solutions that fit the data with the smallest stressing rates that is as close to zero stress rate prior as possible. Previous work has suggested that the subduction zone is locked to 10–17 km depth [*Hyndman and Wang*, 1995; *Flück et al.*, 1997; *McCaffrey et al.*, 2007]. Here we solve for the locking depth by adding a constraint to the shear stress rate inversion

$$\min ||\boldsymbol{\Sigma}^{-1/2}(\mathbf{G}\mathbf{A}^{-1}\dot{\boldsymbol{\tau}} - \mathbf{d})||_2^2 + \alpha^2||\dot{\boldsymbol{\tau}}_{\mathbf{z}>\mathbf{z}_{\max}}||_2^2 \quad \text{s.t.} \quad \dot{\mathbf{s}}_{\mathbf{z}<\mathbf{z}_{\max}} = \mathbf{0} \tag{8}$$

Note that as now posed the fault is locked above $z_{\max}$, and the minimum shear stress rate applies only to the creeping fault below the locked zone. For a given locking depth $z_{\max}$, we solve this inverse problem using the MATLAB-built least squares solver lsqlin, and for each value of α^2, the square of the regularization parameter, we store the root-mean-square of the residuals to the entire data set (horizontal and vertical) and the root-mean-square of the residuals to the vertical rates only. To allow additional flexibility in the inversion and to improve the fit to the long-term rates, we extend the model fault to 80 km depth.

Figure 11 displays the resulting curves for each locking depth as a function of the regularization parameter α. Nine values of locking depth $z_{\max}$ are considered, ranging from 0 km (no imposed locking) to 25 km (5 km above the ETS region). Considering all models that fit the full data set to within 1 mm/yr excludes models with locking depth greater than 21 km; these models have larger misfits for all values of α. Note that for $\alpha < 1.5 \times 10^{-4}$ the solution is too rough to be realistic. The model with the deepest locking depth that fits the data adequately thus has a locking depth of 21 km. For this locking depth all models with $\alpha < 2.95 \times 10^{-4}$ fit the data to within 1 mm/yr. Of these models the one with the lowest average stressing rate within the ETS zone is the one with $\alpha = 2.95 \times 10^{-4}$.

Figure 11a shows that there is a family of shallower locking depths (19 km and lower) that fit the data as well or even better than for a 21 km locking depth. However, these models do not fit the uplift rates as well, as shown in Figure 11b. The models with locking depths between 21 and 23 km have minimum root-mean-square residual to the vertical velocities, fitting these data to on average better than 0.4 mm/yr. Since we previously excluded the solution with 23 km locking depth, our preferred model, which adequately fits both the entire

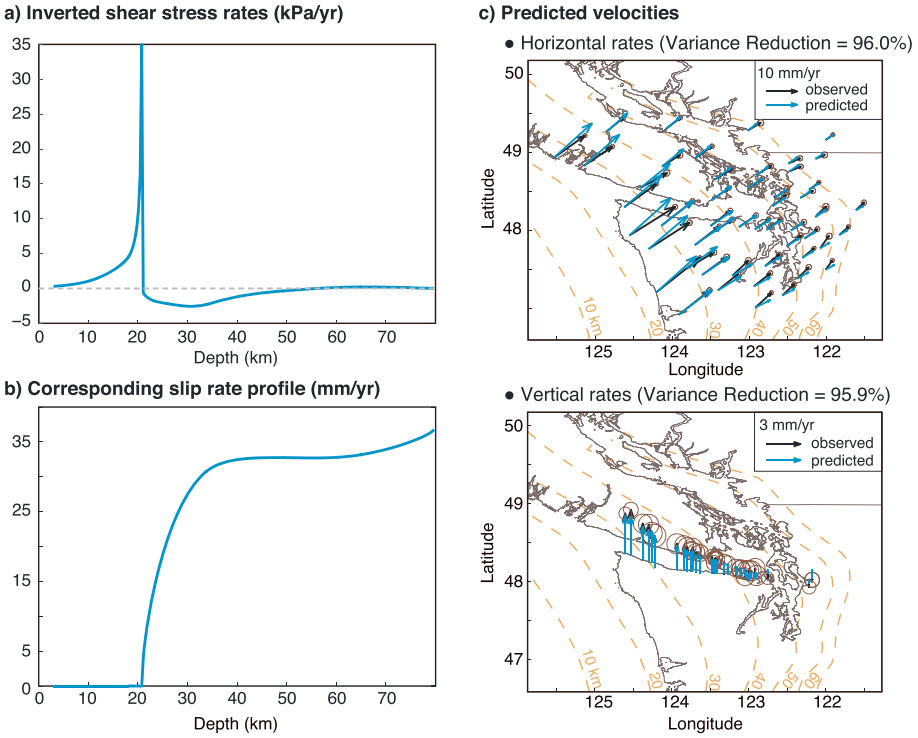

Figure 12. Preferred model from the inversion for shear stress rates with a locking depth of 21 km. (a) Inverted shear stress rate profile. The shear stress decreases with time between 21 km and 50 km, i.e., within the gap and ETS region, reaching −2.5 kPa/yr between 25 and 30 km. (b) Corresponding slip rate profile. (c) Observed and predicted rates.

data set as well as the uplift rates, is the one with the 21 km locking depth. While this model is not unique, it provides a useful guide to physically plausible models that acceptably fit the data.

Figure 12 displays the inferred distributions of stress rate and slip rate and the corresponding fits to the data. The shear stress rate (Figure 12a) shows a strong concentration at the base of the locked zone and negative values immediately below the locking depth. The shear stress rate reaches a minimum around −2.5 kPa/yr between 25 and 30 km. The associated slip rate profile (Figure 12b) is locked between the trench and 21 km (as constrained), followed by a steep increase at 21 km. The result shown in Figure 12 confirms that in order to reproduce the steep slip rate gradient at the top of the ETS region, inferred from Figure 10, the shear stress rates must be negative within the ETS zone. The fit to the uplift rates is greatly improved (Figure 12c) relative to models with constant stress within the ETS zone. The 95% confidence interval on shear stress rate at 25–30 km depth is ± 0.025 kPa/yr, computed by linear propagation of errors, conditioned on a fixed locking depth and regularization parameter. Realistic uncertainties must be much larger, given that a range of locking depths and regularization are largely consistent with the data.

Notice that there are an infinite number of models that fit the full data set better, with less regularization (Figure 11a). However, those models do not fit the vertical data particularly well (Figure 11b). Figure 13 displays the shear stress and the corresponding slip distribution for one of those models, one with no imposed locking depth and less regularization; it is indicated by the dark circle in Figure 11. Some shallow creep, about 5 mm/yr, up to the trench is inferred. Importantly, a slight decrease in shear stress within the top of the ETS zone, reaching −2 kPa/yr at a depth of 30 km, is still observed. Negative shear stress rates in this region steepen the slip rate profile, which is required to improve the fit to the vertical rates at the coastal stations. Nevertheless, this model underpredicts the uplift along the Juan de Fuca Strait. Because there is no locked zone the positive stressing rate in the slip-deficient zone is more subdued relative to that in Figure 12.

5. Discussion

In the previous section we showed that the long-term deformation rates can be best explained by a megathrust locked to around 20 km, with a region of decreasing shear stress between ~20 km and ~40 km (Figure 12).

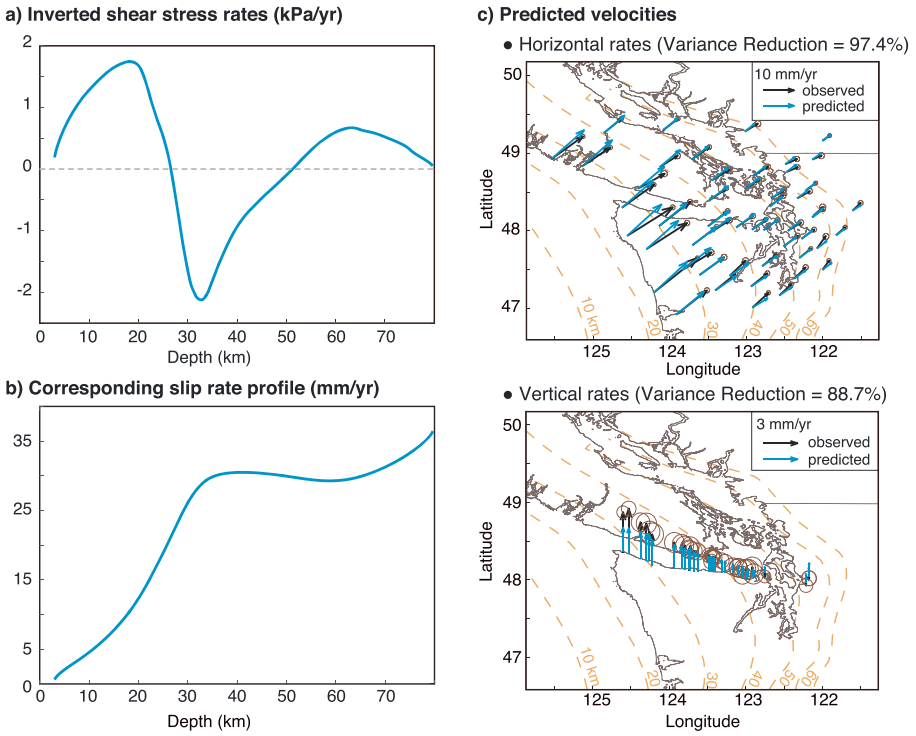

Figure 13. Results of the inversion for shear stress rates for model without imposed locking depth. (a) Inverted shear stress rate profile. The shear stress decreases with time between 25 and 50 km, reaching −2 kPa/yr at 30 km. (b) Corresponding slip rate profile. (c) Observed and predicted rates. Note that the predictions still cannot capture the high uplift rates at the western side of the Olympic Peninsula.

Although this particular solution is not unique, it appears to embody characteristics of all models that reasonably well fit the data, including the uplift rates. The ETS zone lies within the region of negative shear stress rates, between ∼30 km and ∼45 km. As the data favor deeper locking depths, the gap is constrained to the region of high long-term slip rates updip of the ETS region, ∼20–30 km depth. The inversions do not constrain the mechanical behavior of this region but confirm that it is creeping, while ETS events are located on a deeper part of the fault (Figure 14).

As seen in section 3.2, a velocity-strengthening region updip of the ETS region allows the long-term slip rate profile to extend updip but does not change its overall shape. Therefore, we cannot exclude the possibility that the gap exhibits velocity-strengthening behavior. If the gap exhibits velocity-strengthening friction, it might explain why ETS events, after nucleating downdip, do not propagate into the gap as discrete events. Future modeling will be required to test this hypothesis.

Our analysis is heavily influenced by fitting the long-term interseismic vertical rates, assuming that they can be solely explained by elastic deformation. In subduction zones, uplift rates can be affected by inelastic

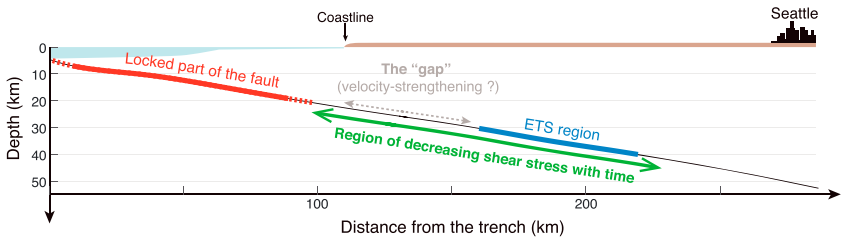

Figure 14. Schematic cross section of the Cascadia megathrust. The long-term surface rates can be best explained by a deep locking depth, around 20 km, and a region of decreasing shear stress from 20–25 km down to 50–60 km, which includes both the gap and the ETS region.

deformation of the accretionary wedge [*Matsu'ura and Sato*, 1989]. In northern Cascadia, *Pazzaglia and Brandon* [2001] showed that bedrock incision rates, a proxy for uplift rates, follow a bell-shaped profile, varying from less than 0.1 mm/yr at the coast to 0.9 mm/yr in the central Olympic range. The westernmost coastal stations, which are critical in our analysis, are minimally affected by inelastic deformation. Furthermore, the amplitude of the uplift due to inelastic deformation is small compared to observed interseismic rates. Even at the maximum where inelastic uplift rates reach 0.9 mm/yr, it accounts for less than a third of the contemporary rate at the corresponding longitude. Although inelastic deformation does not appear to explain either the shape or the amplitude of the observed uplift rates along the Strait of Juan de Fuca, this effect warrants further investigation.

This work assumes fully elastic response, as most analyses of interseismic deformation; however, it is well known that viscoelastic relaxation can alter the deformation field if the Maxwell relaxation time is smaller than the earthquake cycle time [*Savage and Prescott*, 1978; *Wang et al.*, 2012]. *Kim et al.* [2012] explored the hypothesis that viscoelastic earthquake cycle effects could bias the comparison to the geodetic observations, using essentially the same data as examined here. Viscoelastic effects did improve the fit to the horizontal velocities, but they were not able to explain the long-term vertical deformation rates.

Shear stress acting on the megathrust plane τ is the product of the effective normal stress $\bar{\sigma} = \sigma_n - p$ and the coefficient of friction μ, $\tau = \mu\bar{\sigma}$. A temporal decrease in τ could thus suggest a reduction in the coefficient of friction μ or in effective normal stress $\bar{\sigma}$, due to increasing pore pressure p. From Darcy's law and the conservation of fluid mass, pore pressure satisfies a diffusion equation of the form

$$\rho S_s \frac{\partial p}{\partial t} = \nabla \left[\left(\frac{k\rho}{\nu} \right) \cdot (\nabla p - \rho g) \right] + \rho\Gamma \tag{9}$$

where ρ is the fluid density, S_s the specific storage, k the permeability, ν the fluid viscosity, and Γ a source or sink of pore pressure. At steady state, the diffusion term balances the source term Γ, such that $\partial p/\partial t = 0$. In subduction zones mechanical pore compaction and metamorphic reactions are known to release water-rich fluids along the plate interface [*Peacock*, 2009; *Saffer and Tobin*, 2011; *Saffer and Wallace*, 2015; *Audet and Kim*, 2016]. Increasing dehydration reactions increases the source term Γ, potentially leading to a positive $\partial p/\partial t$. While past studies have concluded that the ETS zone is not associated with a single metamorphic phase transition or temperature [*Peacock*, 2009; *Saffer and Wallace*, 2015], the region where we infer negative shear stress rates is not limited to the ETS region (Figure 14). In fact, the largest decrease in shear stress is observed between 20–25 and 35 km depth, in the gap right above the ETS zone (Figures 12–14). Dehydration reactions could take place in this depth range, which corresponds roughly to the transition from greenschist to epidote amphibolite facies [*Hacker et al.*, 2003; *Peacock*, 2009]. Furthermore, although often considered to occur only at phase boundaries, dehydration reactions are also known to occur within facies domains, far from metamorphic boundaries [*Peacock*, 2009]. *Skarbek and Rempel* [2016] have recently discussed the role of chemical dehydration within the viscously deforming subduction channel in generating migrating pore pressure changes.

The shear stress rate inversion predicts a change of −2.5 kPa/yr within the ETS zone. If this is due to a change in effective normal stress, might this alter the SSE characteristics over the long term that could be detected? For instance, a simple model for SSE recurrence interval T depends on effective normal stress $\bar{\sigma}$ and the stressing rate $\dot{\tau}$

$$T = \frac{\Delta\tau}{\dot{\tau}} \propto \frac{\bar{\sigma}}{\dot{\tau}} \tag{10}$$

where $\Delta\tau$ is the stress drop during a slow-slip event. Decreasing $\bar{\sigma}$ with time suggests a decrease in the recurrence interval between slow-slip events. Considering the assumed low normal stress in the ETS region, a few megapascal, and a recurrence interval of 15 months in northern Cascadia [*Szeliga*, 2004; *Brudzinski and Allen*, 2007], the recurrence interval should decrease by a few days between slow-slip events. Because of the natural variability in the occurrence of slow-slip events as well as along-strike variability, this effect could be easily missed in observations.

The temporal evolution of the shear stress τ could also be caused by a long-term weakening of the fault, i.e., a reduction of the coefficient of friction μ within the gap. A second, larger slip-weakening distance D_c in both

the gap and the ETS region might also weaken the fault over the long term as more slip accumulates; however, it is unclear whether such a model can be made consistent with the observations.

We showed that the best fitting model favors locking depths close to 20–21 km. This result differs from previous estimates of between 10–17 km [*Hyndman and Wang*, 1995; *Flück et al.*, 1997; *McCaffrey et al.*, 2007; *Burgette et al.*, 2009]. One difference lies in the fact that, in our study, we use an updated 3-D fault model from *McCrory et al.* [2012]. Compared to previous slab models, such as the ones presented in *McCrory et al.* [2006], it exhibits a steeper profile close to the trench. Therefore, although the depth is greater, the distance to the trench remains roughly the same. In map view, the locking depths described in past studies follow the coastline in Northern Washington and so does our inferred locking depth (Figure 14).

Our data-driven results contrast with simple physics-based models that predict roughly constant shear stress within the SSE zone when averaged over many SSE cycles. Specifically, the long-term velocities, particularly the vertical, require a shear stress decrease within the gap and the updip part of the ETS zone. The magnitude of the shear stress change is surprising given the inference of low ambient effective normal stresses at these depths [*Audet et al.*, 2009; *Audet and Bürgmann*, 2014]. Supposing that the effective normal stresses are on the order of 1 MPa, and $\mu \sim 0.6$, a stationary decrease in shear stress of 2.5 kPa/yr would lead to zero effective normal stress on the megathrust after 240 years. Certainly, there is no evidence that the inferred shear stress rate was held for all times since the last megathrust event, but this result remains puzzling. Future work should provide an explanation for this curious behavior by finding physics-based mechanisms that reconcile the inversion predictions with the numerical modeling.

6. Conclusions

Physics-based models with velocity-weakening friction and low effective stress in the ETS zone fit average ETS displacements well but predict too much locking when compared to decadal-averaged surface velocities. Possible bias due to use of homogeneous half-space Green's functions is unlikely to explain the misfit. A velocity-strengthening region above the ETS zone permits creep within the gap between the locked and ETS zones, improving the fit to horizontal velocities, but fails at explaining the observed uplift rates. Minimum norm inversions of the residuals from these models show that larger slip rates are necessary between 22 and 50 km, suggesting nonstationary shear stress rates within both the gap and the ETS zone. We invert for the distribution of shear stress rate on the megathrust, with the fault locked to a variable depth and nonzero shear stress rate penalized below the locked zone. We find that negative shear stress rates within both the gap and the ETS region, reaching −2.5 kPa/yr at a depth of ∼25–30 km, are required. Of all the models that adequately fit both horizontal and vertical data, only those with deep locking depths, around 21 km, significantly improve the fit to the uplift rates.

Acknowledgments
This work was supported by the U.S. Geological Survey (G15AP00066). GPS data used in this study are made available by PANGA, the Pacific Northwest Geodetic Array, Central Washington University (http://www.geodesy.cwu.edu/data/bysite). The leveling and tide gauge data sets were made available in *Krogstad et al.* [2016]. Simulations were done using the quasi-dynamic code FDRA. Code and input files to reproduce simulation results are available upon request. We thank Reed Burgette, Ray Weldon, and Randy Krogstad for providing us the leveling and tide gauge data early on and the two anonymous reviewers for their insightful comments.

References

Aagaard, B. T., M. G. Knepley, and C. A. Williams (2013), A domain decomposition approach to implementing fault slip in finite-element models of quasi-static and dynamic crustal deformation, *J. Geophys. Res. Solid Earth*, *118*, 3059–3079, doi:10.1002/jgrb.50217.

Atwater, B. F. (1987), Evidence for great Holocene earthquakes along the outer coast of Washington State, *Science*, *236*(4804), 942–944, doi:10.1126/science.236.4804.942.

Atwater, B. F., et al. (1995), Summary of coastal geologic evidence for past great earthquakes at the Cascadia Subduction Zone, *Earthquake Spectra*, *11*, 1–18, doi:10.1193/1.1585800.

Audet, P., and R. Bürgmann (2014), Possible control of subduction zone slow-earthquake periodicity by silica enrichment, *Nature*, *509*(7505), 389–392, doi:10.1038/nature13391.

Audet, P., and Y. Kim (2016), Teleseismic constraints on the geological environment of deep episodic slow earthquakes in subduction zone forearcs: A review, *Tectonophysics*, *670*, 1–15, doi:10.1016/j.tecto.2016.01.005.

Audet, P., M. G. Bostock, N. I. Christensen, and S. M. Peacock (2009), Seismic evidence for overpressured subducted oceanic crust and megathrust fault sealing, *Nature*, *457*(7225), 76–78, doi:10.1038/nature07650.

Bartlow, N. M., S. Miyazaki, A. M. Bradley, and P. Segall (2011), Space-time correlation of slip and tremor during the 2009 Cascadia slow slip event, *Geophys. Res. Lett.*, *38*, L18309, doi:10.1029/2011GL048714.

Brechet, Y., and Y. Estrin (1994), The effect of strain rate sensitivity on dynamic friction of metals, *Scr. Metall. Mater.*, *30*(11), 1449–1454, doi:10.1016/0956-716X(94)90244-5.

Brudzinski, M. R., and R. M. Allen (2007), Segmentation in episodic tremor and slip all along Cascadia, *Geology*, *35*(10), 907–910, doi:10.1130/G23740A.1.

Burgette, R. J., R. J. Weldon, and D. a. Schmidt (2009), Interseismic uplift rates for western Oregon and along-strike variation in locking on the Cascadia subduction zone, *J. Geophys. Res.*, *114*, B01408, doi:10.1029/2008JB005679.

Dmitrieva, K., and P. Segall (2015), Network-based estimation of time-dependent noise in GPS position time series, *J. Geod.*, *89*, 591–606, doi:10.1007/s00190-015-0801-9.

Dragert, H. (2001), A silent slip event on the deeper Cascadia subduction interface, *Science*, *292*(5521), 1525–1528, doi:10.1126/science.1060152.

Dragert, H., and K. Wang (2011), Temporal evolution of an episodic tremor and slip event along the northern Cascadia margin, *J. Geophys. Res.*, *116*, B12406, doi:10.1029/2011JB008609.
Dragert, H., K. Wang, and G. Rogers (2004), Geodetic and seismic signatures of episodic tremor and slip in the northern Cascadia subduction zone, *Earth Planets Space*, *56*(12), 1143–1150, doi:10.1186/BF03353333.
Flück, P., R. D. Hyndman, and K. Wang (1997), Three-dimensional dislocation model for great earthquakes of the Cascadia Subduction Zone, *J. Geophys. Res.*, *102*(B9), 20,539–20,550, doi:10.1029/97JB01642.
Ghosh, A., J. E. Vidale, and K. C. Creager (2012), Tremor asperities in the transition zone control evolution of slow earthquakes, *J. Geophys. Res.*, *117*, B10301, doi:10.1029/2012JB009249.
Goldfinger, C., C. H. Nelson, and J. E. Johnson (2003), Holocene earthquake records from the Cascadia subduction zone and northern San Andreas Fault based on precise dating of offshore turbidites, *Annu. Rev. Earth Planet. Sci.*, *31*(1), 555–577, doi:10.1146/annurev.earth.31.100901.141246.
Hacker, B. R., G. A. Abers, and S. M. Peacock (2003), Subduction factory 1. Theoretical mineralogy, densities, seismic wave speeds, and H_2O contents, *J. Geophys. Res.*, *108*(B1), 2029, doi:10.1029/2001JB001127.
Hawthorne, J. C., and a. M. Rubin (2013), Short-time scale correlation between slow slip and tremor in Cascadia, *J. Geophys. Res. Solid Earth*, *118*, 1316–1329, doi:10.1002/jgrb.50103.
He, C., Z. Wang, and W. Yao (2007), Frictional sliding of gabbro gouge under hydrothermal conditions, *Tectonophysics*, *445*(3-4), 353–362, doi:10.1016/j.tecto.2007.09.008.
Heki, K., S. Miyazaki, and H. Tsuji (1997), Silent fault slip following an interplate thrust earthquake at the Japan Trench, *Nature*, *386*(6625), 595–598, doi:10.1038/386595a0.
Holtkamp, S., and M. R. Brudzinski (2010), Determination of slow slip episodes and strain accumulation along the Cascadia margin, *J. Geophys. Res.*, *115*, B00A17, doi:10.1029/2008JB006058.
Hu, Y., and K. Wang (2012), Spherical-Earth finite element model of short-term postseismic deformation following the 2004 Sumatra earthquake, *J. Geophys. Res.*, *117*, B05404, doi:10.1029/2012JB009153.
Hyndman, R. D. (2013), Downdip landward limit of Cascadia great earthquake rupture, *J. Geophys. Res. Solid Earth*, *118*, 5530–5549, doi:10.1002/jgrb.50390.
Hyndman, R. D., and K. Wang (1995), The rupture zone of Cascadia great earthquakes from current deformation and the thermal regime, *J. Geophys. Res.*, *100*(B11), 22,133–22,154, doi:10.1029/95JB01970.
James, T. S., E. J. Gowan, I. Wada, and K. Wang (2009), Viscosity of the asthenosphere from glacial isostatic adjustment and subduction dynamics at the northern Cascadia subduction zone, British Columbia, Canada, *J. Geophys. Res.*, *114*, B04405, doi:10.1029/2008JB006077.
Kim, M. J., P. Segall, and K. M. Johnson (2012), Constraining interseismic deformation in the Cascadia subduction zone using a viscoelastic earthquake cycle model, Abstract G43B-0926 presented at 2012 Fall Meeting, AGU, San Francisco, Calif., 3–7 Dec.
Krogstad, R. D., D. A. Schmidt, R. J. Weldon, and R. J. Burgette (2016), Constraints on accumulated strain near the ETS zone along Cascadia, *Earth Planet. Sci. Lett.*, *439*, 109–116, doi:10.1016/j.epsl.2016.01.033.
Liu, Y. (2013), Numerical simulations on megathrust rupture stabilized under strong dilatancy strengthening in slow slip region, *Geophys. Res. Lett.*, *40*, 1311–1316, doi:10.1002/grl.50298.
Liu, Y., and J. R. Rice (2009), Slow slip predictions based on granite and gabbro friction data cored to GPS measurements in northern Cascadia, *J. Geophys. Res.*, *114*, B09407, doi:10.1029/2008JB006142.
Lowry, A. R., K. M. Larson, V. Kostoglodov, and R. Bilham (2001), Transient fault slip in Guerrero, Southern Mexico, *Geophys. Res. Lett.*, *28*(19), 3753–3756, doi:10.1029/2001GL013238.
Matsu'ura, M., and T. Sato (1989), A dislocation model for the earthquake cycle at convergent plate boundaries, *Geophys. J. Int.*, *96*(1), 23–32, doi:10.1111/j.1365-246X.1989.tb05247.x.
McCaffrey, R., A. I. Qamar, R. W. King, R. Wells, G. Khazaradze, C. A. Williams, C. W. Stevens, J. J. Vollick, and P. C. Zwick (2007), Fault locking, block rotation and crustal deformation in the Pacific Northwest, *Geophys. J. Int.*, *169*(3), 1315–1340, doi:10.1111/j.1365-246X.2007.03371.x.
McCaffrey, R., R. W. King, S. J. Payne, and M. Lancaster (2013), Active tectonics of northwestern U.S. inferred from GPS-derived surface velocities, *J. Geophys. Res. Solid Earth*, *118*, 709–723, doi:10.1029/2012JB009473.
McCrory, P. A., J. L. Blaire, D. H. Oppenheimer, and S. R. Walter (2006), Depth to the Juan de Fuca slab beneath the Cascadia subduction margin—A 3-D model for sorting earthquakes, U.S. Geol. Surv. Data for Series 91, Version 1.2. [Available at http://pubs.usgs.gov/ds/91.]
McCrory, P. A., J. L. Blair, F. Waldhauser, and D. H. Oppenheimer (2012), Juan de Fuca slab geometry and its relation to Wadati-Benioff zone seismicity, *J. Geophys. Res.*, *117*, B09306, doi:10.1029/2012JB009407.
Mitchell, C. E., P. Vincent, R. J. Weldon, and M. A. Richards (1994), Present-day vertical deformation of the Cascadia Margin, Pacific Northwest, United States, *J. Geophys. Res.*, *99*(B6), 12,257–12,277, doi:10.1029/94JB00279.
Obara, K. (2011), Characteristics and interactions between non-volcanic tremor and related slow earthquakes in the Nankai subduction zone, southwest Japan, *J. Geodyn.*, *52*(3-4), 229–248, doi:10.1016/j.jog.2011.04.002.
Okubo, P. G. (1989), Dynamic rupture modeling with laboratory-derived constitutive relations, *J. Geophys. Res.*, *94*(B9), 12,321–12,335, doi:10.1029/JB094iB09p12321.
Pazzaglia, F. J., and M. T. Brandon (2001), A fluvial record of long-term steady-state uplift and erosion across the Cascadia forearc high, western Washington State, *Am. J. Sci.*, *301*(4-5), 385–431, doi:10.2475/ajs.301.4-5.385.
Peacock, S. M. (2009), Thermal and metamorphic environment of subduction zone episodic tremor and slip, *J. Geophys. Res.*, *114*, B00A07, doi:10.1029/2008JB005978.
Rogers, G., and H. Dragert (2003), Episodic tremor and slip on the Cascadia Subduction Zone: The chatter of silent slip, *Science*, *300*(5627), 1942–1943, doi:10.1126/science.1084783.
Ruina, A. (1983), Slip instability and state variable friction laws, *J. Geophys. Res.*, *88*(B12), 10,359–10,370, doi:10.1029/JB088iB12p10359.
Saffer, D. M., and H. J. Tobin (2011), Hydrogeology and mechanics of subduction zone forearcs: Fluid flow and pore pressure, *Annu. Rev. Earth Planet. Sci.*, *39*, 157–186, doi:10.1146/annurev-earth-040610-133408.
Saffer, D. M., and L. M. Wallace (2015), The frictional, hydrologic, metamorphic and thermal habitat of shallow slow earthquakes, *Nat. Geosci.*, *8*(8), 594–600, doi:10.1038/ngeo2490.
Satake, K. (2003), Fault slip and seismic moment of the 1700 Cascadia earthquake inferred from Japanese tsunami descriptions, *J. Geophys. Res.*, *108*(B11), 2535, doi:10.1029/2003JB002521.
Satake, K., K. Shimazaki, Y. Tsuji, and K. Ueda (1996), Time and size of a giant earthquake in Cascadia inferred from Japanese tsunami records of January 1700, *Nature*, *379*(6562), 246–249, doi:10.1038/379246a0.
Savage, J. C., and W. H. Prescott (1978), Asthenosphere readjustment and the earthquake cycle, *J. Geophys. Res.*, *83*(B7), 3369–3376, doi:10.1029/JB083iB07p03369.

Schmalzle, G. M., R. McCaffrey, and K. C. Creager (2014), Central Cascadia subduction zone creep, *Geochem. Geophys. Geosyst.*, *15*(4), 1515–1532, doi:10.1002/2013GC005172.
Schmidt, D. A., and H. Gao (2010), Source parameters and time-dependent slip distributions of slow slip events on the Cascadia subduction zone from 1998 to 2008, *J. Geophys. Res.*, *115*, B00A18, doi:10.1029/2008JB006045.
Segall, P. (2010), *Earthquake and Volcano Deformation*, Princeton Univ. Press, Princeton, N. J.
Segall, P., and A. M. Bradley (2010), Numerical simulation of slow slip and dynamic rupture in the Cascadia Subduction Zone, Abstract S13D-05 presented at 2010 Fall Meeting, AGU, San Francisco, Calif., 13–17 Dec.
Segall, P., and A. M. Bradley (2012a), Slow-slip evolves into megathrust earthquakes in 2D numerical simulations, *Geophys. Res. Lett.*, *39*, L18308, doi:10.1029/2012GL052811.
Segall, P., and A. M. Bradley (2012b), The role of thermal pressurization and dilatancy in controlling the rate of fault slip, *J. Appl. Mech.*, *79*(3), 31013, doi:10.1115/1.4005896.
Shibazaki, B., and T. Shimamoto (2007), Modelling of short-interval silent slip events in deeper subduction interfaces considering the frictional properties at the unstable—Stable transition regime, *Geophys. J. Int.*, *171*(1), 191–205, doi:10.1111/j.1365-246X.2007.03434.x.
Skarbek, R. M., and A. W. Rempel (2016), Dehydration-induced porosity waves and episodic tremor and slip, *Geochem. Geophys. Geosyst.*, *17*(2), 442–469, doi:10.1002/2015GC006155.
Szeliga, W. (2004), Southern Cascadia episodic slow earthquakes, *Geophys. Res. Lett.*, *31*, L16602, doi:10.1029/2004GL020824.
Wang, K., Y. Hu, and J. He (2012), Deformation cycles of subduction earthquakes in a viscoelastic Earth, *Nature*, *484*(7394), 327–332, doi:10.1038/nature11032.
Wech, A. G. (2010), Interactive tremor monitoring, *Seismol. Res. Lett.*, *81*(4), 664–669, doi:10.1785/gssrl.81.4.664.
Wech, A. G., and N. M. Bartlow (2014), Slip rate and tremor genesis in Cascadia, *Geophys. Res. Lett.*, *41*(2), 392–398, doi:10.1002/2013GL058607.
Wech, A. G., and K. C. Creager (2011), A continuum of stress, strength and slip in the Cascadia subduction zone, *Nat. Geosci.*, *4*(9), 624–628, doi:10.1038/ngeo1215.
Wech, A. G., K. C. Creager, and T. I. Melbourne (2009), Seismic and geodetic constraints on Cascadia slow slip, *J. Geophys. Res.*, *114*, B10316, doi:10.1029/2008JB006090.